



Master's thesis  
Astrophysical Sciences

# Supermassive black holes and the cosmological formation of massive early-type galaxies (title not final)

Atte Keitaanranta

August 12, 2021

Supervisor(s): Prof. Peter Johansson  
M.Sc. Matias Mannerkoski

Censor(s): Prof. Peter Johansson

UNIVERSITY OF HELSINKI  
DEPARTMENT OF PHYSICS  
PL 64 (Gustaf Hällströmin katu 2)  
00014 University of Helsinki



Tiedekunta — Fakultet — Faculty	Koulutusohjelma — Utbildningsprogram — Education programme			
Faculty of Science	Department of Physics			
Tekijä — Författare — Author				
Atte Keitaanranta				
Työn nimi — Arbetets titel — Title				
Supermassive black holes and the cosmological formation of massive early-type galaxies (title not final)				
Opintosuunta — Studieinriktning — Study track				
Astrophysical Sciences				
Työn laji — Arbetets art — Level	Aika — Datum — Month and year	Sivumäärä — Sidoantal — Number of pages		
Master's thesis	August 12, 2021	0 pages		
Tiivistelmä — Referat — Abstract				
Abstract goes here.				
Avainsanat — Nyckelord — Keywords				
Your keywords here				
Säilytyspaikka — Förvaringsställe — Where deposited				
Muita tietoja — övriga uppgifter — Additional information				

# Contents

<b>1</b>	<b>Introduction</b>	<b>1</b>
1.1	Information about galaxies, shortly . . . . .	1
1.2	Aim of the thesis . . . . .	1
<b>2</b>	<b>Background</b>	<b>2</b>
2.1	Cosmology . . . . .	2
2.1.1	Hubble parameter, Friedmann equations and so on . . . . .	2
2.1.2	Cosmological perturbations . . . . .	2
2.2	Early-type galaxies . . . . .	2
2.2.1	Types of ellipticals . . . . .	2
2.2.2	Photometric and kinematic profiles . . . . .	2
2.3	Evolution of dark matter halos . . . . .	2
2.3.1	The Zel'Dovich approximation . . . . .	2
2.4	Feedback processes . . . . .	2
<b>3</b>	<b>GADGET-3 and KETJU</b>	<b>3</b>
3.1	Overview of GADGET-3 . . . . .	3
3.2	Smoothed Particle Hydrodynamics . . . . .	3
3.3	Gas cooling? . . . . .	3
3.4	Feedback? . . . . .	3
3.5	KETJU . . . . .	3

<b>4 Creating initial conditions for the cosmological simulations</b>	<b>4</b>
4.1 Zoom-in technique . . . . .	4
4.2 MUSIC . . . . .	6
4.2.1 Overview . . . . .	6
4.2.2 Generation of the seed density field . . . . .	6
4.2.3 Creation of nested grids . . . . .	10
4.2.4 Particle displacements and velocity fields . . . . .	12
4.3 Cosmological setup for the GADGET-3 zoom-in and KETJU simulations . . . . .	14
4.4 Methods for locating regions of interest . . . . .	15
4.4.1 Identifying halos: Friends-of-friends algorithm . . . . .	15
4.4.2 Locating centers of objects: Shrinking sphere method . . . . .	16
<b>5 Cosmological GADGET-3 zoom-in simulations</b>	<b>18</b>
5.1 Low-resolution run . . . . .	18
5.2 Overview of the cosmological zoom-in simulations . . . . .	20
5.3 Analysis of the properties of the galaxies . . . . .	24
5.3.1 Virial information . . . . .	24
5.3.2 Rotation curves . . . . .	24
5.3.3 Star formation . . . . .	27
5.3.4 Colors and magnitudes . . . . .	29
5.4 Locating starting points for KETJU . . . . .	29
<b>6 Simulations with KETJU</b>	<b>32</b>
<b>7 Conclusions</b>	<b>33</b>
<b>Bibliography</b>	<b>33</b>

# **1. Introduction**

**1.1 Information about galaxies, shortly**

**1.2 Aim of the thesis**

## **2. Background**

### **2.1 Cosmology**

**2.1.1 Hubble parameter, Friedmann equations and so on**

**2.1.2 Cosmological perturbations**

### **2.2 Early-type galaxies**

**2.2.1 Types of ellipticals**

**2.2.2 Photometric and kinematic profiles**

### **2.3 Evolution of dark matter halos**

**2.3.1 The Zel'Dovich approximation**

### **2.4 Feedback processes**

# **3. GADGET-3 and KETJU**

- Haven't really thought about the contents of this chapter yet

## **3.1 Overview of GADGET-3**

## **3.2 Smoothed Particle Hydrodynamics**

## **3.3 Gas cooling?**

## **3.4 Feedback?**

## **3.5 KETJU**

# 4. Creating initial conditions for the cosmological simulations

This chapter describes how the initial conditions (ICs) for cosmological simulations are created. The first section describes the so-called ‘zoom-in’ method, which allows us to have spatially large simulation boxes with high resolution regions. After this, the code MUSIC (MULTi-Scale Initial Conditions) is introduced, which is used to create a spatial volume with realistic velocity and density perturbations at an early redshift ( $z = 50$ ). Compared to an earlier implementation by Bertschinger (2001), the errors in the velocity and displacement fields are improved by two orders of magnitude (Hahn & Abel, 2011). The created initial ICs are used as a starting point for the performed GADGET-3 simulations that are run in this thesis. The last part of this chapter focuses on the setup of the cosmological setup of the simulations, and how the output of the preliminary low resolution large volume run is analyzed to find regions of interest needed for the higher resolution simulation.

## 4.1 Zoom-in technique

To study galaxy formation and evolution in a proper cosmological context, the simulation box must have a large volume. The perturbations at multiple fundamental length scales enter the non-linear regime at different redshifts and thus without a large enough volume (spatial dimensions of the box being  $\sim 100 \text{ Mpc}$ ), the matter power spectrum is not resolved correctly on the largest scales. This results in unrealistic gravitational tidal forces from the large scale structures, which in turn create incorrect peculiar velocities in smaller scale structures, as shown in e.g. Mo et al. (2010).

To resolve the gravitational effects of a smaller scale structure, it is also required to have a high resolution, i.e. a large amount of particles with relatively low mass.

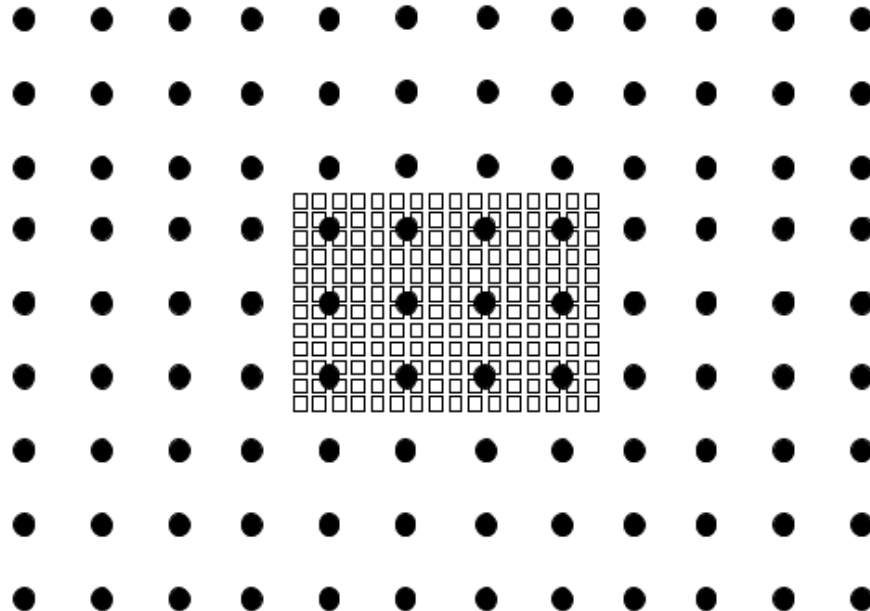


**Figure 4.1:** An example of a zoom-in region, with one level of mesh refinement. The circles represent the particles on the coarse grid. The squares represent the refined particles, with each coarse particle inside this region divided into  $4^3$  particles.

Having a sufficient resolution on the whole simulation volume would result in a unreasonably large computational workload. Thus it is more sensible to implement a method, which has a high resolution in a single region of interest, surrounded by a large volume with a smaller resolution. This method, nowadays known as the ‘zoom-in’ technique, has been in use for multiple decades. One of the first simulations with a region of interest surrounded by low resolution background was performed by Navarro & White (1994), and later implementations have been used by e.g. Power et al. (2003) and Marinacci et al. (2014) to name a few.

An example of a zoom-in grid is shown in Figure 4.1. Here, the dots represent the large particles on a coarse grid, while the crosses represent the refined grid with lower mass particles. In this refinement, each massive particle in the refined region is divided into  $4^3$  particles. Modern implementations, such as the one used in this thesis, use zoom regions with multiple levels of refinement (see Section 4.2.3). As adding levels of refinement resolves smaller structures, the results of zoom-in simulations with different maximum resolution change slightly. The simulation with better resolution includes more low-mass satellites, and their locations can also differ. The masses of most massive objects are also affected, and mergers can occur at slightly different times.

To locate the regions of interest, we need to first perform a computationally less expensive simulation without a high resolution volume (discussed in 5.1) including only dark matter, and then choose the zoom-in regions and perform the simulation again with baryons included. The initial conditions (ICs) must also portray a realistic case, i.e. the fluctuations at a very high redshift must match the expected density structure from linear theory. As the redshift is till very high ( $z > 20$ ), the evolution of density structures is still following the linear theory. Fortunately, we can use a single program to create realistic ICs, with zoom-in box included.

## 4.2 Music

### 4.2.1 Overview

MUSIC (MUlti-Scale Initial Conditions) is a code written by Hahn & Abel (2011), which can be used to create the ICs for GADGET-3 simulations. The program creates a simulation volume, with velocity and particle displacements calculated using a power spectrum and two-point correlation given as input. To account for fluctuations on smaller scales, the program is also able to create a high resolution zoom-in region for the ICs. The zoom-in region can have multiple levels of refinement, and an example of an IC created using MUSIC is shown in Figure 4.2.

MUSIC improves on the prior work, e.g. the GRAFIC-2 code made by Bertschinger (2001), which also produces ICs with multiple levels of refinement. One of most notable upgrades in MUSIC compared to GRAFIC-2 is the way the transfer function is used to calculate the density perturbations, discussed in 4.2.2. Another improvement is the way different refinement levels constrain other levels, which is discussed in 4.2.3.

The initial conditions produced by the code best describe the velocity and density structure when the redshift of the produced ICs lie on the linear perturbation regime. If the initial redshift  $z_i$  of the ICs is set to be too low (i.e. on the non-linear regime), the formation of the first haloes occurs at unrealistically late times and the formation of high-mass haloes is suppressed, as shown by Reed et al. (2013). Still, MUSIC gives relatively accurate ICs even in the mildly non-linear regime of  $z_i \sim 20$  (Hahn & Abel, 2011).

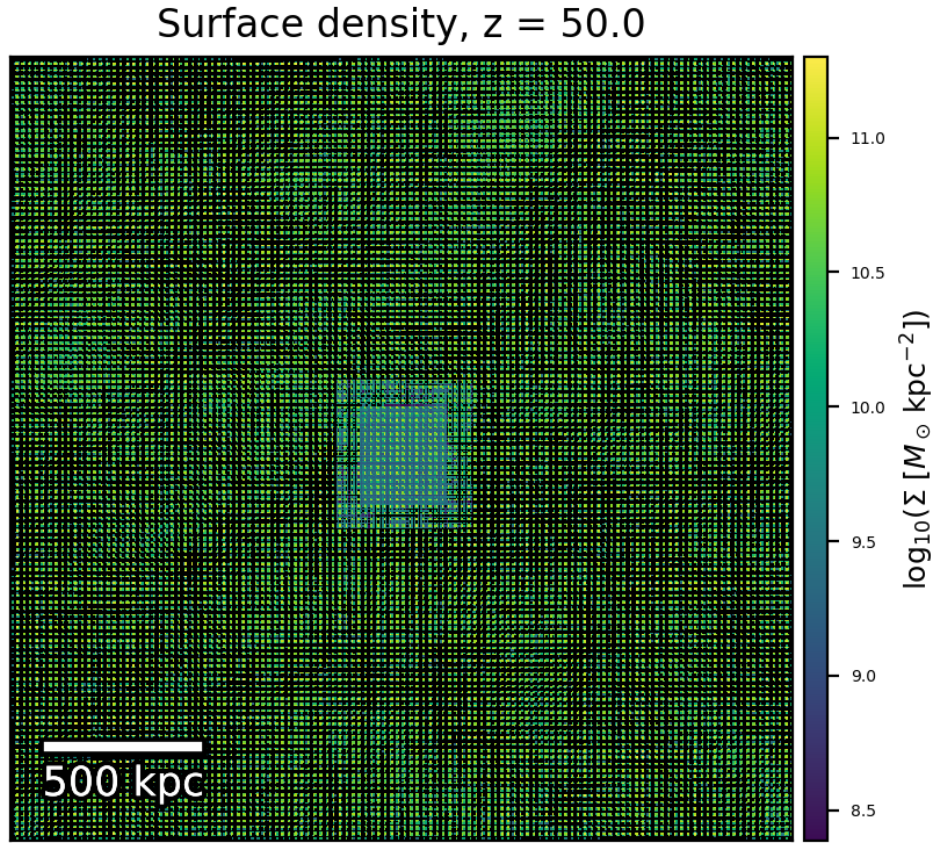


**Figure 4.2:** An example of a density field created using MUSIC, in physical units. The sidelength of the simulation box is 100 Mpc/h. At the center, a region with four refinement levels is included.

### 4.2.2 Generation of the seed density field

For the generation of particle velocities and positions, MUSIC first needs to create a density field, described by a density perturbation  $\delta(\mathbf{r})$ . Using an a Power spectrum  $P(k)$  given as input, this field can be described completely, as the power spectrum of the field is given by

$$P(k) \equiv \langle \tilde{\delta}(\mathbf{k}) \tilde{\delta}^*(\mathbf{k}) \rangle, \quad (4.1)$$

where  $*$  denotes the complex conjugate, and  $\tilde{\delta}(\mathbf{k})$  represents the Fourier transform of the density perturbation, i.e.

$$\tilde{\delta}(\mathbf{k}) = \int \delta(\mathbf{x}) e^{-i\mathbf{k}\cdot\mathbf{x}} d^3\mathbf{x}. \quad (4.2)$$

The transfer function  $T(k)$  can also be used to express the power spectrum, defined as

$$P(k) = \alpha k^{n_s} (T(k))^2, \quad (4.3)$$

where  $\alpha$  is a constant used to normalize the power spectrum, and  $n_s$  is the spectral index, describing the slope of the spectrum. The value of the spectral index is given to MUSIC in the configuration file, while  $\alpha$  is evaluated via the observable value of the variance of the galaxy distribution  $\sigma^2$  at a distance  $R$ .

For the distribution of galaxies, as shown in e.g. Mo et al. (2010), the predicted variance is defined as

$$\sigma^2(R) = \frac{1}{2\pi^2} \int P(k) \tilde{W}^2(k) k^2 dk, \quad (4.4)$$

where  $\tilde{W}(k)$  is defined as the Fourier transform of a window function  $W(r)$ . There are multiple choices for the window function, and the most popular one is the top-hat window function  $W(r)$ , which is given by

$$W(r) = \begin{cases} \frac{3}{4\pi R^3}, & r \leq R \\ 0, & r > R. \end{cases} \quad (4.5)$$

The Fourier transform of this function is

$$\tilde{W}(k) = \frac{3}{(kR)^3} (\sin(kR) - kR \cos(kR)). \quad (4.6)$$

As the variance, as well as the shape of the power spectrum are known, the amplitude of the spectrum can now be normalized. For historical reasons, the distance where the variance is usually measured is  $R = 8 \text{ Mpc/h}$ , and is also the value MUSIC takes as input to normalize the power spectrum. At this distance,  $\sigma(8 \text{ Mpc/h}) \equiv \sigma_8$  is valued close to unity, since this is approximately the length scale at which the structure evolution becomes non-linear, with structures having higher length scales evolving linearly [SOURCE].

As the shape of the power spectrum are known and the spectrum is normalized, the generation of the density field is now possible. The goal is to create the density field from random noise values  $\mu(\mathbf{r})$ , while requiring that the amplitudes follow the power spectrum  $P(k)$ . The sample of random values  $\mu(\mathbf{r})$  is called the white noise sample. White noise field is a field which with an constant power spectrum, i.e.  $P(k) \propto k^n$  with  $n = 0$  (Mo et al., 2010).

MUSIC generates the white noise sample using a Gaussian distribution. Detailed discussion of Gaussian distributions can be found in multiple sources of literature, for example Mo et al. (2010). For a distribution to be Gaussian, the probability density function  $\varrho$  of random value  $x$  is

$$\varrho(x) = \frac{1}{\sqrt{2\pi}\sigma} \exp\left(-\frac{(x - \bar{x})^2}{2\sigma^2}\right), \quad (4.7)$$

where  $\bar{x}$  and  $\sigma^2$  are the mean and the variance, respectively. This equation can be generalized to higher dimensions, and for a  $n$ -dimensional random field  $\delta(\mathbf{x}) = (\delta_1, \delta_2, \dots, \delta_n)$  the distribution is Gaussian if the probability distribution function can be written as

$$\varrho(\delta_1, \delta_2, \dots, \delta_n) = \frac{1}{\sqrt{(2\pi)^n \det(\mathcal{M})}} e^{-\mathcal{L}}, \quad (4.8)$$

where  $\mathcal{M}$  is the covariance matrix,  $\mathcal{M}_{ij} = \langle \delta_i \delta_j \rangle$ , and

$$\mathcal{L} \equiv \frac{1}{2} \sum_{i,j} \delta_i (\mathcal{M}^{-1})_{ij} \delta_j. \quad (4.9)$$

It is assumed that the Gaussian random field is homogenous and isotropic, meaning that the multivariate Gaussian distribution functions are invariant under spatial translation or rotation. Therefore the two-point correlation function  $\xi(r)$  completely determines the distribution functions. Specifically, the field's one-point distribution function is

$$\varrho(\delta) d\delta = \frac{1}{\sqrt{2\pi\sigma^2}} e^{-\frac{\delta^2}{2\sigma^2}} d\delta, \quad (4.10)$$

where the variance of the field is  $\langle \delta^2(\mathbf{x}) \rangle = \sigma^2 = \xi(0)$ . Note: Peter, you mentioned that I should explain a bit what  $\xi(0)$  means, but I'm struggling with this. Is there a book/paper I could check or could you explain a bit what  $\xi(0)$  means?

Returning to the white noise sample, the amplitudes of the random values  $\mu(\mathbf{r})$  can be generated to follow the power spectrum  $P(k)$  by considering the Fourier transformed random field  $\tilde{\mu}(\mathbf{k})$ . With this, the Fourier transformed field  $\tilde{\delta}(\mathbf{k})$  can be written as

$$\tilde{\delta}(\mathbf{k}) = \sqrt{P(||\mathbf{k}||)} \tilde{\mu}(\mathbf{k}) = \alpha ||\mathbf{k}||^{n_s/2} T(||\mathbf{k}||) \tilde{\mu}(\mathbf{k}). \quad (4.11)$$

A common procedure to evaluate the real-space density field is to perform an inverse Fourier transform to  $\tilde{\delta}(\mathbf{k})$ , as is done in e.g. Bertschinger (2001). MUSIC uses a different approach, and calculates the real-space density field as

$$\delta(\mathbf{r}) = \mathcal{T}_R(||\mathbf{r}||) * \mu(\mathbf{r}), \quad (4.12)$$

where  $\mathcal{T}_R(r)$  is the real-space counterpart of  $\tilde{\mathcal{T}}(k) \equiv \alpha k^{n_s/2} T(k)$  and "\*" is denoting a convolution, discussed thoroughly by Salmon (1996). Briefly, the white noise  $\mu(\mathbf{x})$  is realised as density perturbations in real space using the convolution operator. This method has previously been used by e.g. Pen (1997) and Sirk (2005). Hahn & Abel (2011) also show that previous implementations that use the inverse Fourier transform of  $\delta(\mathbf{k})$  results in too small values for the two-point correlation function.

To calculate the  $\delta(\mathbf{r})$  via convolution, it is till required to transform  $\tilde{\mathcal{T}}(k)$  into real space, which MUSIC achieves by performing the calculation (assuming that  $\tilde{\mathcal{T}}(k)$  is spherically symmetric)

$$\mathcal{T}_R(r) = \frac{1}{(2\pi)^3} \int_{\mathbb{R}} \tilde{\mathcal{T}}(k) e^{i\mathbf{x}\cdot\mathbf{k}} \cdot \mathbf{k} d^3\mathbf{k} \quad (4.13)$$

$$= \frac{1}{2\pi^2} \int_0^\infty \tilde{\mathcal{T}}(k) \frac{\sin(kr)}{kr} dk. \quad (4.14)$$

### 4.2.3 Creation of nested grids

When creating the refined regions, the white noise of the subgrids must be consistent with the white noise og the coarse domain, meaning that when dividing a particle (parent cell) into smaller particles (children cells), the mass must be conserved. A common way to achieve this has been the Hofmann-Ribak algorithm (Hoffman & Ribak, 1991), which GRAFIC-2 also uses.

The Hofmann-Ribak algorithm first creates individually white noise fields  $w^\ell$  and  $w^{\ell+1}$ . The field with higher level of refinement is unconstrained at this point and has a variance 8 times higher than the one level coarses  $\ell$ . Having 8 times higher variance is equivalent to dividing the parent cells into groups eight children cells. To match the level  $\ell + 1$  to  $\ell$ , the mean white noise of the finer level must be matched to the value of the coarser level. Bertschinger (2001) achieves this by subtracting the mean of the unconstrained sample from the sum of the coarse white noise and the unconstrained white noise.

While this algorithm does conserve the mass of the coarse grid on the finer subgrids, the approach does not preserve the Fourier modes of the coarse white noise. Thus MUSIC uses a modified method, which still utilizes the Hofmann-Ribak algorithm while retaining the Fourier modes.

When creating the refined subgrids, the method still divides each parent cell into eight children cells. A two-dimensional example of this is shown in Figure 4.3. After this, the Fourier modes of the coarse grid are preserved by performing a Fast Fourier Transform (FFT) of the transfer function on two regions: on the fine grid, and on the coarse grid region which is overlapping with the finer grid. For the finer grid, all of the modes up to the so-called Nyquist wave of the coarse grid,  $\mathbf{k} \leq \mathbf{k}_{Ny}$ , are then replaced by with the modes of the coarse level. The value of the Nyquist wave number is  $k_{Ny} = \pi/\Delta x$ , where  $\Delta x$  is the spacing of the particles on the coarse grid. This value acts as a cutoff value for the FFT, as numerical calculations of Fourier transformations cannot be continued to infinity.

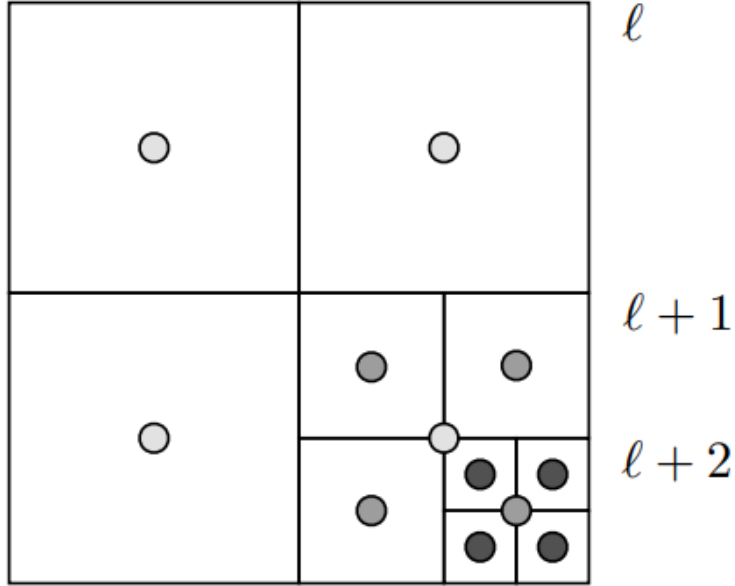


**Figure 4.3:** A two dimensional example layout of multiple scale nested grid (Hahn & Abel, 2011). The figure shows parent cells on level  $\ell$ , and children cells on two higher levels. The center of the children cells is not in the same position as the center of the parent cell.

The Fourier modes are now preserved, and an inverse Fourier transform can be performed to create the a refined subgrid with perserved Fourier modes. Finally, a reverse version of the Holfmann-Ribak algorithm is used. With this, average of the children cells on the finer level define and replace the the white noise values of the coarser level on the overlapping regions.

With multiple levels of refined subgrids present, this method is started from the finest subgrid, and moving to coarser grids one level at a time. In the regions where levels  $\ell$  and  $\ell + 1$  overlap, the parent cells are replaced by the average of the eight children cells and thus, in addition to conserving the Fourier modes, the mass is conserved.

To calculate the over-density fields on each level of the nested grids using FFTs, the convolution kernels  $T(r)$  are still needed for all refined levels. For this, the levels of the nested grid are divided into domains  $\Omega_\ell$  and each domain is surrounded by a padded domain  $\Omega_{\ell,p}$ . The sides of the padded domain are double the length compared to the domain  $\Omega_\ell$ , as shown in Figure 4.4. The padded domain is needed to keep the Fourier transforms isolated, which leads to conservation of the wave modes when performing the convolution.

The creation of convolution kernels starts from the finest level  $\ell$ . At this level,

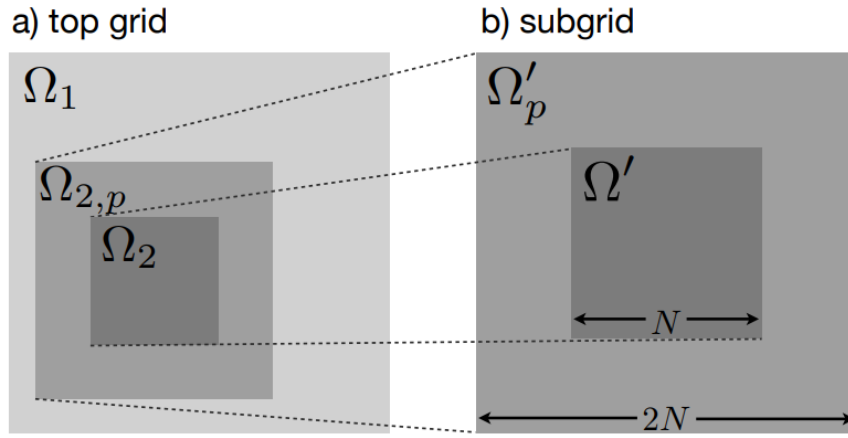


**Figure 4.4:** A two-dimensional representation of domains of two levels of refinement, including the padded domain for the subgrid. The domain of the higher resolution level has a sidelength of  $N$ , and the padded domain has a sidelength of  $2N$  (Hahn & Abel, 2011).

the convolution kernel in the domain and the padded domain is simply equivalent to the real-space transfer function,

$$T^\ell(\mathbf{x}) = \mathcal{T}_R(||\mathbf{x}||), \quad (4.15)$$

where  $\mathcal{T}_R$  is evaluated as shown in eq. 4.14. The origin is placed at the center of the domain. For the next level, the calculation of the kernel is performed in two different ways, depending on the location for which the kernel is evaluated at. If the location on the level does not have a refined subgrid over it, the calculation for the kernel is performed in the same way as for the most refined level, as shown in eq. 4.15. As mentioned before, for the overlapping regions, the kernels all averaged over the eight children cells. This is achieved with the calculation

$$T^{\ell-1}(\mathbf{x}) = T^{\ell-1}(x, y, z) = \frac{1}{8} \sum_{i,j,k \in \{-\frac{\Delta x^\ell}{2}, \frac{\Delta x^\ell}{2}\}} T^\ell(x + i, y + j, z + k), \quad (4.16)$$

where  $\Delta x^\ell$  is the spacing of the particles on level  $\ell$ . The relation of the spacing of particles in refinement levels  $\ell$  and  $\ell - 1$  is  $\Delta x^{\ell-1}/\Delta x^\ell = 2$ . After level  $\ell - 1$ , the calculation of kernels moves on to level  $\ell - 2$ , and so on. For these, the kernels are calculated the same way as for level  $\ell - 1$ .

#### 4.2.4 Particle displacements and velocity fields

Note: I'll explain more about the Zeldovich approximation on chapter 2

The generated density field from the white noise sample is used as a starting point for the evolution of particle position and velocity fields. The evolution is calculated using the Lagrangian perturbation theory. Time evolution of position and velocity of each fluid element (i.e. each particle) is followed until the initial redshift  $z_i$  is reached. The time evolution of the density field "displaces" particles, turning the initial Gaussian field into a non-Gaussian field.

In Lagrangian perturbation theory, the time evolution of position  $\mathbf{x}(t)$  and velocity  $\mathbf{v}(t)$  is determined by a so-called "displacement field"  $\mathbf{L}(\mathbf{q}, t)$ , where  $\mathbf{q}$  is the initial position of a particle. The time evolution of position and velocity is written as

$$\mathbf{x}(t) = \mathbf{q} + \mathbf{L}(\mathbf{q}, t), \quad (4.17)$$

$$\mathbf{v}(t) = \frac{d\mathbf{L}(\mathbf{q}, t)}{dt}. \quad (4.18)$$

For the numerical calculation of the displacement field, MUSIC uses the first order approximation, the so-called Zel'Dovich approximation (Zel'Dovich (1970), see also 2.3.1). With this, the displacement field can be calculated as

$$\mathbf{L}(\mathbf{q}, t) = -\frac{2}{3H_0^2 a^2 D(t)} \nabla \phi(\mathbf{q}, t) \equiv D^{-1}(t) \nabla \Phi(\mathbf{q}, t), \quad (4.19)$$

where  $D(t)$  is the growth factor of linear density perturbations and  $\Phi$  is the potential, whose gradient is proportional to the gradient of the gravitational potential  $\phi$  (Hahn & Abel, 2011). The evolution of the gravitational potential is calculated by solving the Poisson's equation, which is written as

$$\Delta \phi(\mathbf{q}, t) = \frac{3}{2} H_0^2 a^2 \delta(\mathbf{q}, t). \quad (4.20)$$

With this first order approximation, the velocity of each particle is acquired via a gradient of the potential. Thus the velocity field with this approximation results in  $\nabla \times \mathbf{v}(t) = 0$  (Hahn & Abel, 2011). MUSIC is also capable of calculating the fields using a more complicated second order approximation, but it was not used when generating ICs for the simulations in this thesis.

To achieve a numerical solution for the Poisson's equation, MUSIC uses a hybrid of two methods, FFT and a multi-grid solution called Full Approximation Scheme (FAS, Brandt (1977)), solving the equation on the finest grid and proceeding from that to coarser levels. With this hybrid method, the FFT is only used for the finest level.

For the levels in which the Poisson's equation is solved using FAS, the equation is written in the form of

$$\Delta\phi(\mathbf{x}) = f(\mathbf{x}). \quad (4.21)$$

The implementation of FAS in MUSIC is thoroughly explained in the paper by Hahn & Abel (2011). In summary, MUSIC approximates the value of  $\phi$  on grid level  $\ell$  to be  $u^\ell$ , with the operator  $\Delta$  being approximated to Laplacian value  $L$ , taken from a table. These can be used to calculate the residual term  $r^\ell = f^\ell - L^\ell u^\ell$ . This generates two terms affecting level  $\ell - 1$ . The second term generates an additional correction term for the grid at level  $\ell - 1$ . In addition, a restrictive term is present due to the first source term,  $f^\ell$ . To account for these terms, a so-called smoothing scheme  $S(u^\ell, f^\ell)$  is performed, and is applied using the Gauss-Seidel sweep. This method is applied recursively on each level to decrease the value of the residual  $r^\ell$  until a threshold value is reached, resulting in an excellent approximation for the value of  $\phi$  and allowing the program to create the necessary ICs for cosmological simulations.

### **4.3 Cosmological setup for the GADGET-3 zoom-in and KETJU simulations**

The goal of this thesis is to study the output of cosmological simulations performed with GADGET-3 and KETJU. To acquire the simulation data analyzed in chapters 5 and 6, the following steps and runs are performed:

1. Generate an IC without baryons using MUSIC.
2. Run a GADGET-3 simulation from the created IC to redshift  $z = 0$ .
3. Locate areas of interest from the output.
4. Use MUSIC to create ICs with zoom-in regions. Two versions are created: with and without baryons.
5. Perform the zoom-in cosmological runs with GADGET-3.
6. Analyze the output data and starting points for simulations with KETJU enabled.
7. Perform the KETJU runs and analyze the data.

All of the performed simulations use the same cosmological parameters, which are shown in Table 4.1, also including the resulting critical density. These are the default values MUSIC uses, and are very close to observed estimates (Planck Collaboration et al., 2020). In addition, all of the simulations have periodic boundary conditions. The starting redshift of the ICs created with MUSIC is set to  $z_i = 50$  and the sidelength of the box is set to 100 Mpc/h.

$H_0$ (km/s/Mpc)	$\Omega_m$	$\Omega_b$	$\Omega_\Lambda$	$\sigma_8$	$n_s$	$\rho_{\text{crit}}$ (kg/m <sup>3</sup> )
70.3	0.276	0.045	0.724	0.811	0.961	$9.28 \times 10^{-27}$

**Table 4.1:** Cosmological parameters used for the simulations. The critical density acquired with these parameters is also included. If a simulation doesn't include baryons, the dark matter density parameter  $\Omega_{\text{DM}}$  is equal to the matter density parameter  $\Omega_m$ . If baryons are included,  $\Omega_{\text{DM}} = \Omega_m - \Omega_b$ .

The coarse grid is made up of  $128^3$  particles. The matter density can be written as

$$\rho_m = \Omega_m \rho_{\text{crit}} = \frac{Nm}{V}, \quad (4.22)$$

where  $N$  is the number of particles,  $m$  the mass of a single particle and  $V = L^3$  is the volume of the box. Combining this with the equation for critical density (eq. 2.??, added after chapter 2 is written), the mass of a single particle can be calculated with

$$m = \frac{V}{N} \Omega_m \rho_{\text{crit}} = \frac{L^3}{N} \frac{3H(t)^2}{8\pi G} \Omega_m. \quad (4.23)$$

For the simulations performed here, this leads to coarsest particles having a mass of  $3.65 \times 10^{10} M_\odot/h$ .

## 4.4 Methods for locating regions of interest

For the analysis of the cosmological simulations (and to locate regions of interest for the zoom-in simulations), an algorithm is needed to locate halos from the low resolution dark matter only simulation (discussed in 5.1). Here, two methods are shortly introduced. The first is used to divide the simulation particles into groups, each being a halo. The second method is used to find the center of mass of a halo, necessary for the analysis of the formed halos and galaxies.

#### 4.4.1 Identifying halos: Friends-of-friends algorithm

To divide the output data into objects, an algorithm called the Friends-of-Friends (FoF) algorithm is used. Versions of the algorithm have been used for observational surveys and simulation data, e.g. Huchra & Geller (1982) and Nolthenius & White (1987) for survey implementations Davis et al. (1985) and Nurmi et al. (2013) for usage with simulation data, to name a few.

To use the algorithm on the output data, a Python module pygad (Röttgers et al., 2020) is used. With this, the FoF algorithm is used to divide the simulation particles into groups, with each group representing a halo. A particle is considered to be a part of the same group as another particle, if the distance between the two particles is smaller than a determined threshold value  $l$ . This value is often called the linking length and these two particles are called ‘friends’. Similarly, two particles in two individual groups are separated by a length smaller than the linking length, the two groups are combined to one group. An example of two groups defined with FoF is shown in Figure 4.5.

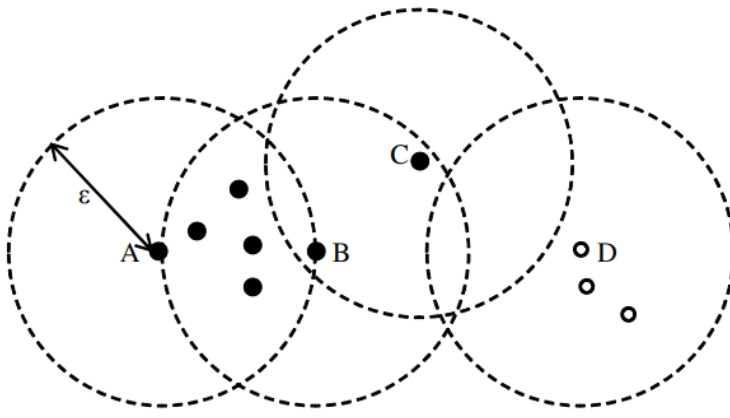


**Figure 4.5:** An example showing two groups defined with the FoF algorithm, as shown in Kwon et al. (2010). Black particles form one group, and the white ones another. For particles A, B, C and D, circles having a radius  $\epsilon$ , which is equal to the linking length is shown. Particles inside the circles are the friends of the central particle. For example, even though particles A and C are not considered friends, they are still part of the same group.

The FoF algorithm is used to find objects using the position of dark matter particles. However, the determined groups do not necessarily represent physical, gravitationally bound structures. Thus the center of a determined group may not coincide with the center of the halo, and another after applying the FoF algorithm, another method is used to locate the centers.

#### 4.4.2 Locating centers of objects: Shrinking sphere method

The centers of the objects defined with the FoF algorithm are calculated with the so-called shrinking sphere method (Power et al., 2003). This method is also applied using pygad (Röttgers et al., 2020).

The method begins with placing a sphere with radius  $r_0$  around the center location of object determined using the FoF algorithm. The new location of the calculated center is then placed at the center of mass of the particles within the sphere. Another, shrunken sphere is then placed at this location with the radius being a few percent smaller than the previous radius. In this thesis, the radius is shrunk by 2.5%.

To find the real center of the object, this method is applied recursively. After each placement of a shrunken sphere, new center of mass is calculated using the particles within the new sphere. These steps are applied recursively until the amount of particles left inside a sphere decreases below a threshold limit. The real center is the final center of mass calculated. Acquiring a great estimate for the center makes it possible to analyse multiple properties of the formed halos and galaxies, like colors and rotations curves, for example.

# 5. Cosmological GADGET-3 zoom-in simulations

On this chapter, the results of the performed cosmological GADGET-3 simulations are described. First, the dark matter only low resolution run is introduced. This run is mainly used to locate the regions in which to place zoom-in regions. Once this is done, overview of the performed cosmological simulations is given, including the computational load of the performed zoom-in simulations and density profiles of the galaxies. Furthermore, the results of the zoom-in simulations are described. These simulations were performed with two different resolutions to determine the affect of resolution on the properties of the formed galaxies. The studied properties of the galaxies include virial information, rotation curves, star formation histories and colors. Finally, the simulation output at various redshifts is studied, with the goal of finding optimal starting points for the KETJU simulations, which are performed to study the mergers of SMBHs in cosmological simulations.

## 5.1 Low-resolution run

The ‘low resolution’ GADGET-3 cosmological simulation including only dark matter was run from redshift  $z = 50$  until current time, redshift  $z = 0$ . This simulation was performed on Kale, which is a computer cluster of University of Helsinki. The run used 16 CPUs on one node, lasting approximately 24 hours and 4 minutes (see also Table 5.1).

To locate regions of interest from the low resolution run, the FoF algorithm is used (see Section 4.4.1). For the linking length, the default value of pygad was used, which is

$$l = \left( \frac{1500 \rho_{\text{crit}}}{m_{\text{DM}}} \right)^{-1/3} \approx 89.8 \text{ ckpc/h}, \quad (5.1)$$

where  $m_{\text{DM}}$  is the mass of a dark matter particle. The goal is to choose multiple

massive dark matter structures with halos in them, and place a zoom-in region on the location where the particles forming the halo are located at the start of the simulation. For this, the center of the halo is estimated to be at the mean position of the particles, since each particle is a dark matter particle of equal mass. Next, we check what is the maximum distance  $r_{\max}$  of a halo particle from the center, and make a sphere of  $1.5 r_{\max}$  over the center. Finally, we take every particle inside this sphere, and trace their locations back to the beginning of the simulation, and check the minima and maxima of the three comoving spatial dimensions of these particles. These values are used as the borderlines of the zoom-in region. Locating the regions of interest is done in comoving coordinates in order to see the initial positions of the particles, compared to the location of the structure they form at reshift  $z = 0$ .

A radius resulting in a sphere covering more than just the located sturcture was used to prevent contaminating the zoom-in halo with massive particles. A large presence of massive particles in the region inside radius  $r$  of a halo can decrease the amount of gas in this inner region by a few percent, as the high mass particles can act as an artificial gravitational sink (Oñorbe et al., 2014).

Three zoom-in regions were chosen from the low resolution run. Figure 5.1 shows the surface density of the whole simulation volume, in comoving coordinates. The three dots show the locations of the chosen halos for the zoom-in simulations. The three boxes show the locations of the placed zoom-in regions at the beginning of the simulation.

For each three cases with refined a volume, simulations are performed with two different resolutions, called medium and high resolution henceforth. The medium resolution run has three levels of refinement, and the high resolution has four. For both resolutions, two runs are performed: a run with only dark matter, and a run with dark matter and gas particles. Thus each of the three zoom-in region is simulated in four different runs, totaling 12 different simulations.

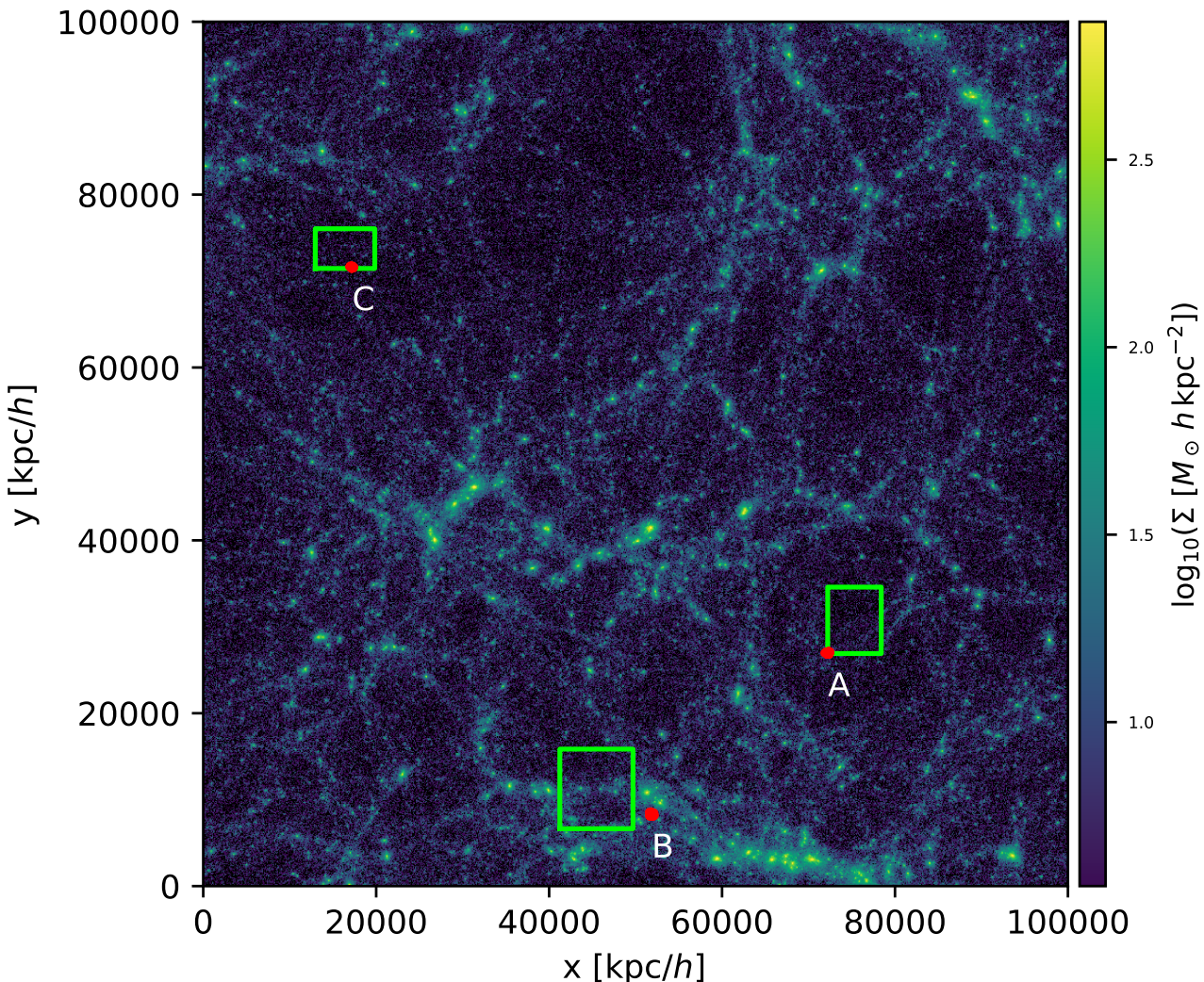


**Figure 5.1:** Surface density of the low resolution cosmological simulation at redshift  $z = 0$ . The red dots show the locations of the three halos which were chosen to be refined in the zoom-in simulations. The three boxes show the initial locations of the particles which form the three halos. The three halos are simply named A, B and C.

## 5.2 Overview of the cosmological zoom-in simulations

All of the GADGET-3 simulations including refined regions were run with the CSC supercomputer Puhti. Each simulation started from redshift  $z = 50$ , and is run until redshift  $z = 0$ . The simulations create output files (called snapshots henceforth) of

the current state of the simulation slightly more often than once every 100 Myr, totaling 150 snapshots. The dark matter only simulations were run on one node using 20 CPUs while the simulations including dark matter and baryons were also run on one node, but using 40 CPUs. The elapsed times, including the low resolution simulation, are shown in table 5.1.

The elapsed times clearly show that computational load is increased when adding baryons or increasing refinement level. Especially in the simulations including baryons, the simulation times are greatly increased with improved resolution, since structures on smaller scales are solved. The computation times for the halo C are the smallest, while the times are largest for halo B. This was expected, as halo B has the largest amount of particles in the low resolution run, and thus has the largest zoom-in region and more small mass particles compared to A and C. Similarly, the halo C was the smallest of the three and thus the fastest to simulate (see the sizes of the zoom-in regions in Figure 5.1).

Simulation	CPUs used	Elapsed real time	CPU time
DM only, low res	16	1 d 4 min	16 d 1 h 4 min
DM only, med res, A	20	2 h 36min	2 d 3 h 52 min
DM only, med res, B	20	3 h 28 min	2 d 21 h 21 min
DM only, med res, C	20	1 h 32 min	1 d 6 h 51 min
DM only, high res, A	20	5 h 55 min	4 d 22 h 27 min
DM only, high res, B	20	11 h 25 min	9 d 12 h 13 min
DM only, high res, C	20	4 h 26 min	3 d 16 h 36 min
Med res, A	40	8 h 44 min	14 d 13 h 30 min
Med res, B	40	16 h 32 min	27 d 13 h 17 min
Med res, C	40	6 h 55 min	11 d 12 h 42 min
High res, A	40	4 d 19 h 37 min	192 d 16 h 30 min
High res, B	40	9 d 17 h 2 min	1 yr 23 d 9 h 4 min
High res, C	40	3 d 8 h 8 min	133 d 13 h 17 min

**Table 5.1:** Computational overview of the simulations performed with GADGET-3 without KETJU. The low resolution dark matter only run was performed using Kale, while the other simulations were run on Puhti.

Another noticeable thing is that the low resolution dark matter only simulation took much longer than the dark matter only simulations with higher resolution. This is caused by a few reasons. First, compared to Kale, the processing units of Puhti are

more powerful. The amount of CPUs was also slightly increased. Another, likely the most important, reason for the faster computations is that the frequency of updating the tree structure was increased. In the low resolution run, the tree is reconstructed after  $0.1 N$  force calculations, where  $N$  is the total amount of particles. For the simulations run with Puhti, this value is set to  $0.01 N$ . This is the only change made to the GADGET-3 parameters after the low resolution simulation. Even though rebuilding the tree structure more frequently obviously adds more computation time, the total time is still decreased. This is most likely caused by an improved balance of computational load between the cores, since updating the trees reallocates the new trees (and the particles in them) to the cores. This way the chance of having a computationally remarkably large load on one core decreases.

In order to give an example of the impact of the addition of one extra refinement level, surface density profiles of the simulations of the galaxy A are shown in Figure 5.2. All four profiles are from the simulations including baryons and dark matter. Smaller scales are resolved in the high resolution simulations and thus, compared to the medium resolution simulation, more small satellites can be seen around the galaxy in the high resolution simulation surface densities. The large scale structure formed by dark matter is also clearly more visible in the high resolution simulation. It is also worth noting that the surface densities are much higher than in Figure 5.1. This is simply caused by the fact that in the Figure 5.1 the whole simulation volume is shown and thus the surface densities are integrated over the whole  $z$ -axis. The maps in Figure 5.2 focus only on the region with refined dark matter particles and gas, and hence the surface densities are only integrated over a slice of the  $z$ -axis.

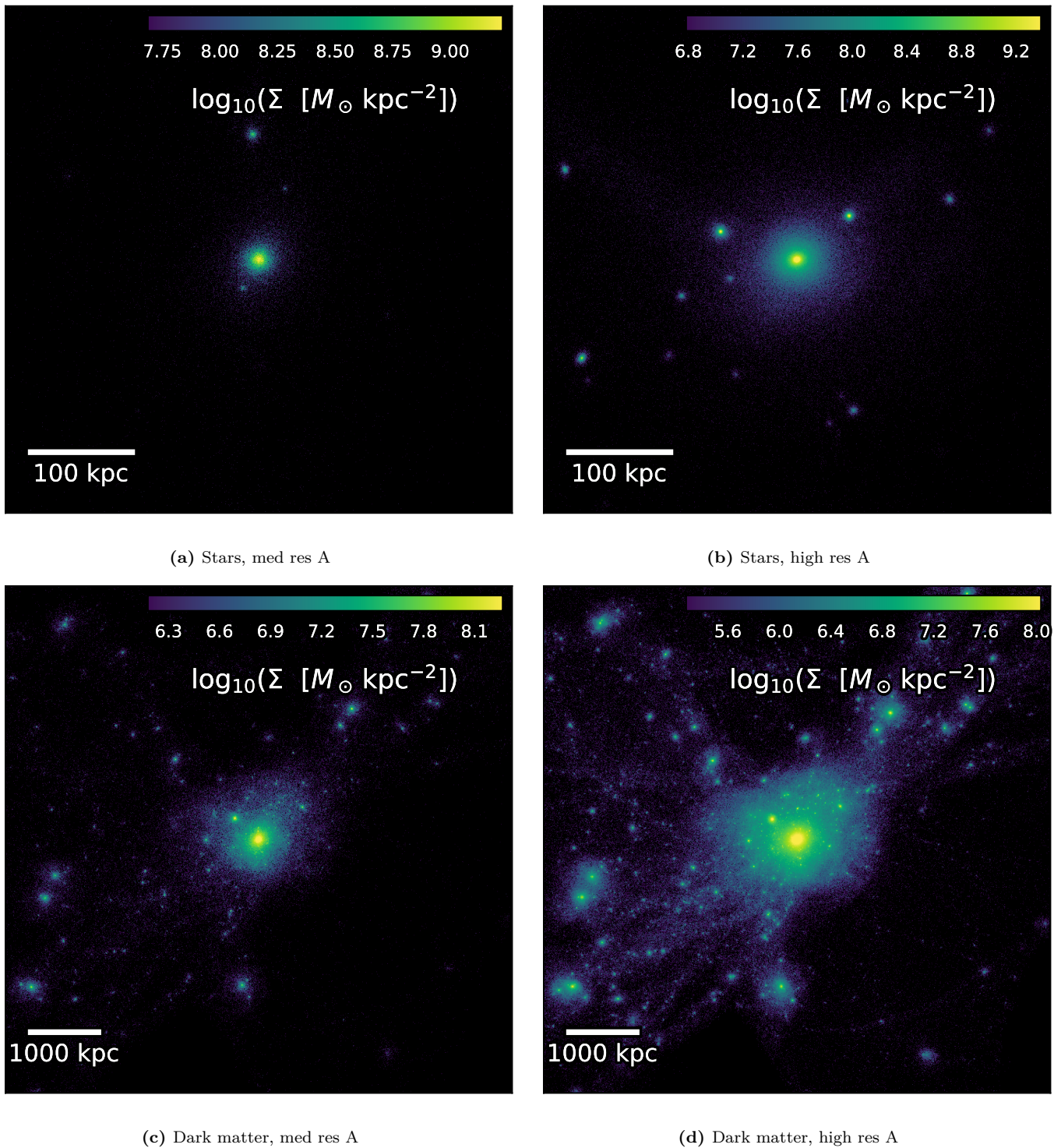


**Figure 5.2:** Surface density profiles for the simulated galaxy A. The upper row shows the stellar surface densities, while the lower row is the surface density of the refined dark matter particles. The center in each figure is set to the location found for the galaxy using the shrinking sphere method. Note: I think I should also show these figures for galaxies B and C, but it would mean that there are only figures for three pages in a row. Is this okay or should I add these figures maybe in the appendix?

## 5.3 Analysis of the properties of the galaxies

### 5.3.1 Virial information

Table 5.2 shows the virial properties of the simulated galaxies. For each three chosen targets, neither one level of refinement nor inclusion of baryons makes a large difference for the virial mass or radius. Here, the virial radius was chosen in the common way, i.e.

$$r_{\text{vir}} = r \left( \frac{\rho(r)}{\rho_{\text{crit}}} = 200 \right). \quad (5.2)$$

The size of the visible galaxy is difficult to determine solely from the output data. Thus, for the analysis performed in this thesis, it is defined that the radius of the galaxy is  $r_{\text{gal}} = 0.1 r_{\text{vir}}$ , similarly to e.g. Johansson et al. (2012). When analysing the star formation and colors of the galaxies (see sections 5.3.3 and 5.3.4, respectively), the stars whose distance from the center is larger than  $r_{\text{gal}}$  are ignored.

Simulation	$r_{\text{vir}}$ (kpc)	$M_{\text{vir}}$ ( $M_{\odot}$ )
DM only, med res, A	517	$1.59 \times 10^{13}$
DM only, high res, A	515	$1.57 \times 10^{13}$
Med res, A	522	$1.64 \times 10^{13}$
High res, A	526	$1.68 \times 10^{13}$
DM only, med res, B	582	$2.27 \times 10^{13}$
DM only, high res, B	581	$2.25 \times 10^{13}$
Med res, B	574	$2.17 \times 10^{13}$
High res, B	578	$2.22 \times 10^{13}$
DM only, med res, C	406	$7.66 \times 10^{12}$
DM only, high res, C	409	$7.86 \times 10^{12}$
Med res, C	401	$7.38 \times 10^{12}$
High res, C	400	$7.36 \times 10^{12}$

**Table 5.2:** Virial properties of the simulated galaxies at redshift  $z = 0$ .

### 5.3.2 Rotation curves

In order to study the masses of the galaxies as a function of radius, it is customary to not to plot the mass, but rather the circular rotation curve  $V_c(r)$ , calculated as

$$V_c(r) = \sqrt{\frac{GM(< r)}{r}}, \quad (5.3)$$

where  $M(< r)$  is the total mass of the system inside radius  $r$ .

The rotation curves for each of the medium and high resolution cosmological simulations at redshift  $z = 0$  are shown in Figure 5.3. Solid lines mark the high resolutions simulations, and the dashed lines represent the medium resolution simulations. In the case of simulations including baryons at redshift  $z = 0$ , the rotation curves are shown for the inner 50 kpc. For dark matter only simulations, the curves are shown up to 100 kpc.

For the cosmological simulations with only dark matter, no large differences are seen between high and medium resolution for any of the simulations. For galaxies B and C, the circular rotation curves are very close to each other up to  $\sim 50$  kpc, with B reaching almost 350 km/s at 100 kpc while the rotation curve for C goes to 300 km/s. The increase of the rotation curve as a function of radius is fastest for the dark matter halo A, which nearly reaches 400 km/s. At the radius of 100 kpc, the growth of the rotation curve for each dark matter only simulation has nearly stagnated. This shape of the dark matter halo is in line with other dark matter only simulations, e.g. Tissera & Dominguez-Tenreiro (1998), for example. The slow growth of the rotation curve of the dark matter only version of galaxy B compared to A is a bit surprising, as the galaxy B has the highest virial mass. This indicates that the space around galaxy B is denser than the volumes around galaxies A and C.

It is easy to see the large effect the inclusion of baryons result in: all three high resolution results show large peaks in the inner regions inside the inner 10 kpc, with rotation curves peaking around 2 – 3 kpc. Both galaxies A and C reach rotation velocities slightly under 500 km/s, while the galaxy B reaches a high velocity of over 600 km/s. Compared to these rotation curves, it is clear that the dark matter only simulations lack the central concentration. Moving outward from the central region, the rotation curves become nearly constant, meaning that  $M \propto r$  at large radii. A noticeable peak in the central region and the nearly constant values at large radii are both expected properties for the rotations curves, as these are seen in observations (Weijmans et al. (2008) and Napolitano et al. (2009), to name a few). The results also agree with other simulations, e.g. Johansson et al. (2012) and Naab et al. (2007), even though the rotation curves presented here, especially the one for galaxy B, reach noticeably higher values compared to these. This is somewhat expected as the virial masses are higher than in the simulations in Johansson et al. (2012) and Naab et al. (2007), and thus the galaxies are also expected to be more massive. The largest peak which reaches 600 km/s is also a reasonable maxima, as

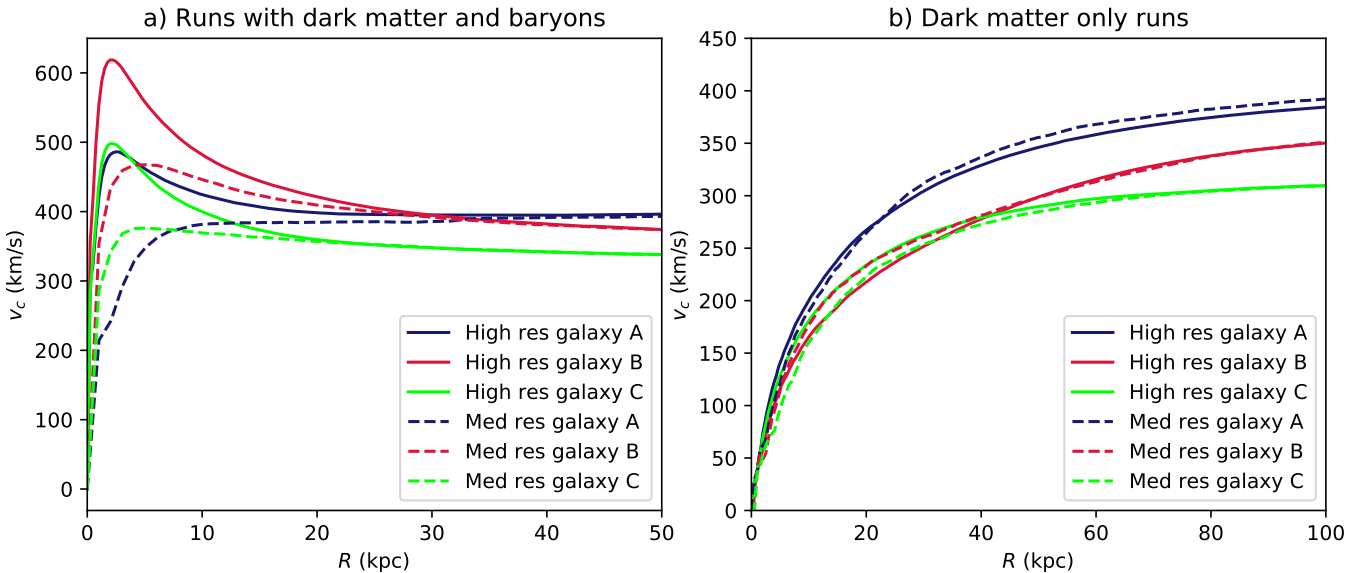


**Figure 5.3:** Rotations curves  $V_c(r)$  of the simulated galaxy for each simulation including baryons and dark matter. Right: Rotation curves from the simulations only including dark matter. The continuous lines represent the high resolution simulations and the dash-dotted lines represent the medium resolution simulations.

peaks as high as 700 km/s have been reached (Meza et al., 2003).

While the result do not significantly vary between the two resolutions in the dark matter only simulations, looking at the rotation curves from the simulations including both baryons and dark matter show that there are clear differences between the two. While the two resolutions result in the same values at high radii, the inner regions are noticeably mismatched. The medium resolution B rotation curve reveals a dense central region, but it still is far off from the high resolution variant. Medium resolution runs for galaxies A and C are practically missing the central peak entirely. These results indicate that the resolution in the medium resolution is not high enough to produce physically reasonable results in the central region.

At earlier times (higher redshifts) the galaxies are expected to be smaller, and the roation curves are shown only for the inner 30 kpc, shown in Figure 5.4. The included rotation curves are acquired from snapshots taken at redshifts 1.0 and 3.0, corresponding to lookback times of 6.62 Gyr and 11.53 Gyr, respectively. Note that the two plots in Figure 5.4 do not have the same upper limit on the y-axis.

Focusing on the high resolution simulations, all three galaxies have a peak which moves to a slightly larger radius as the simulations progress from  $z = 3$  to  $z = 1$ . The peaks also become more spread out, indicating that the size of the stellar part of the galaxy is growing, which is also the case in Johansson et al. (2012). For galaxy B, the maximum of the curve is also greatly incresaing, indicating that more

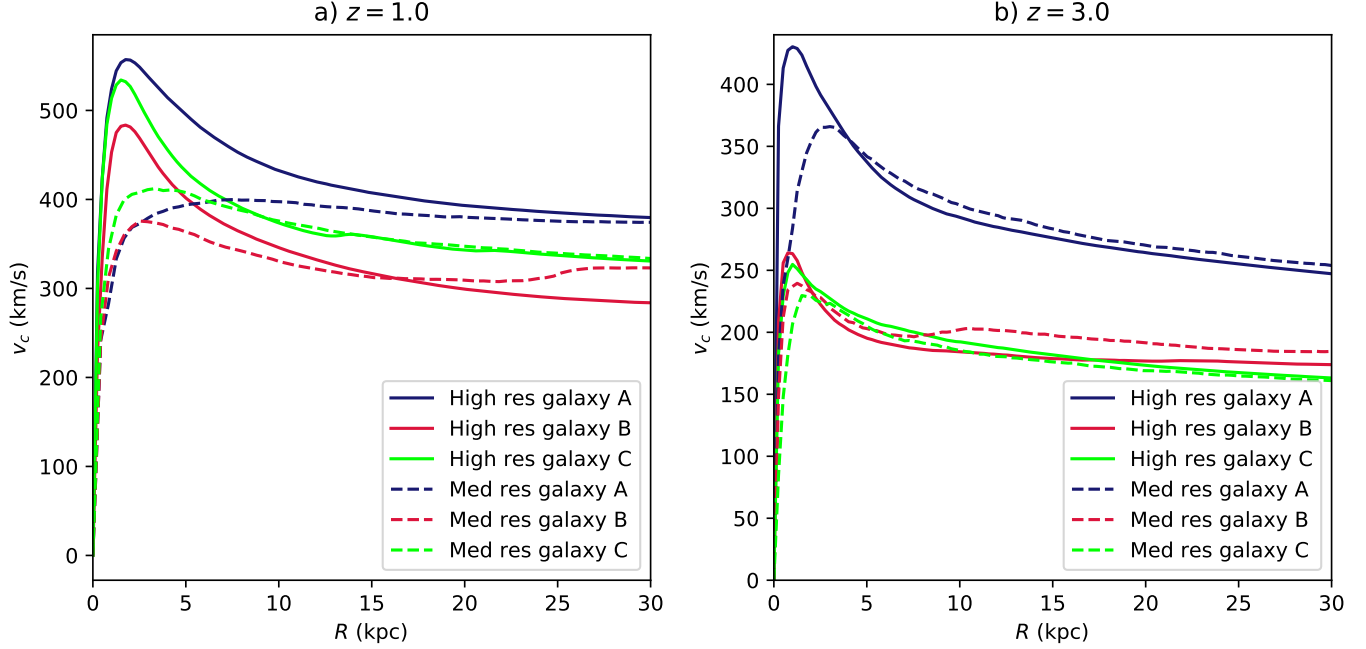


**Figure 5.4:** Left: Rotations curves of the simulated galaxy for each simulation including baryons and dark matter. Left: redshift  $z = 1$ . Right: redshift  $z = 3$ . The continuous lines represent the high resolution simulations and the dasheld lines represent the medium resolution simulations.

matter is accreted to the central region. As the value of the rotation curve  $V_c$  at which of the rotation curve stagnates is higher at redshift  $z = 0$  than at redshift  $z = 1$ , the mass of the galaxy is increasing via mergers. For galaxies A and C, most of the growth occurs before redshift  $z = 1$ , as the changes to the rotation curve is quite similar at redshifts  $z = 0$  and  $z = 1$ . While there are no drastic changes to the mass of the galaxy, the size of their inner regions are increasing, as the maximum of the peaks decreases and the peaks become a bit more spread out.

### 5.3.3 Star formation

- The stellar mass evolution plot is not yet done for high res simulations.
- Redshifts missing from the stellar mass evolution plot
- SFRs, also histograms?
- Again, med res A results will probably change a bit when double precision run is finished.
- Formation efficiencies, comparing to the cosmological parameter

Simulation	$r_{\text{vir}}$ (kpc)	$M_*$ ( $M_\odot$ )	$M_V$ (mag)	$M_{*,\text{gal}}/M_{\text{vir}}$	$M_{\text{bh}}$ ( $M_\odot$ )
Med res, A	517	$3.98 \times 10^{11}$	-22.4	0.025	$5.82 \times 10^9$
Med res, B	574	$5.16 \times 10^{11}$	-22.7	0.024	$6.23 \times 10^9$
Med res, C	400	$2.56 \times 10^{11}$	-22.0	0.035	$3.96 \times 10^9$
High res, A	526	$5.31 \times 10^{11}$	-22.6	0.032	$3.64 \times 10^9$
High res, B	578	$6.38 \times 10^{11}$	-22.8	0.029	$4.54 \times 10^9$
High res, C	400	$3.46 \times 10^{11}$	-22.2	0.047	$2.80 \times 10^9$

**Table 5.3:** Properties of the zoomed-in galaxies at redshift  $z = 0$ .

### 5.3.4 Colors and magnitudes

Test

## 5.4 Locating starting points for KETJU

Test

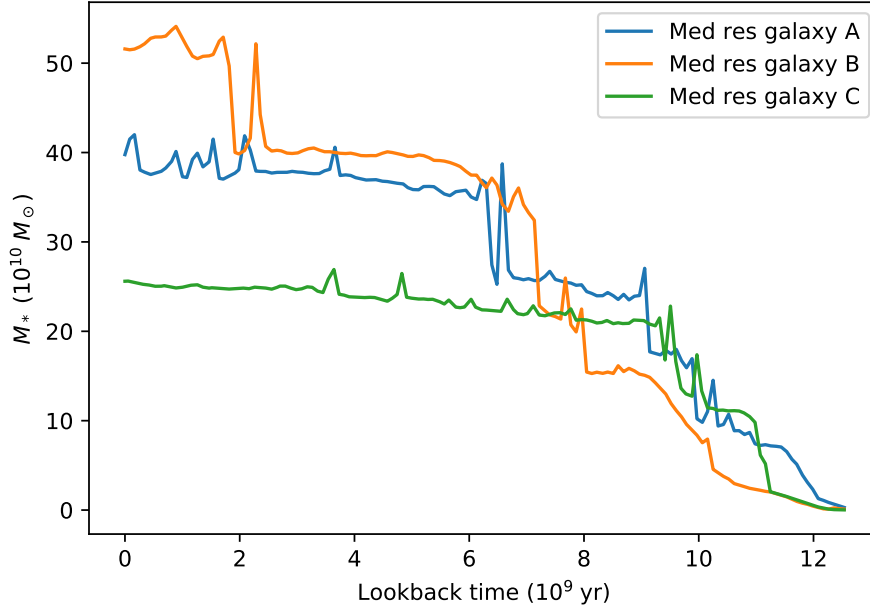


**Figure 5.5:** Stellar mass evolution for the medium resolution galaxies. The calculated stellar mass is the stellar mass within  $r_{\text{gal}} = r_{\text{vir}}/10$ .

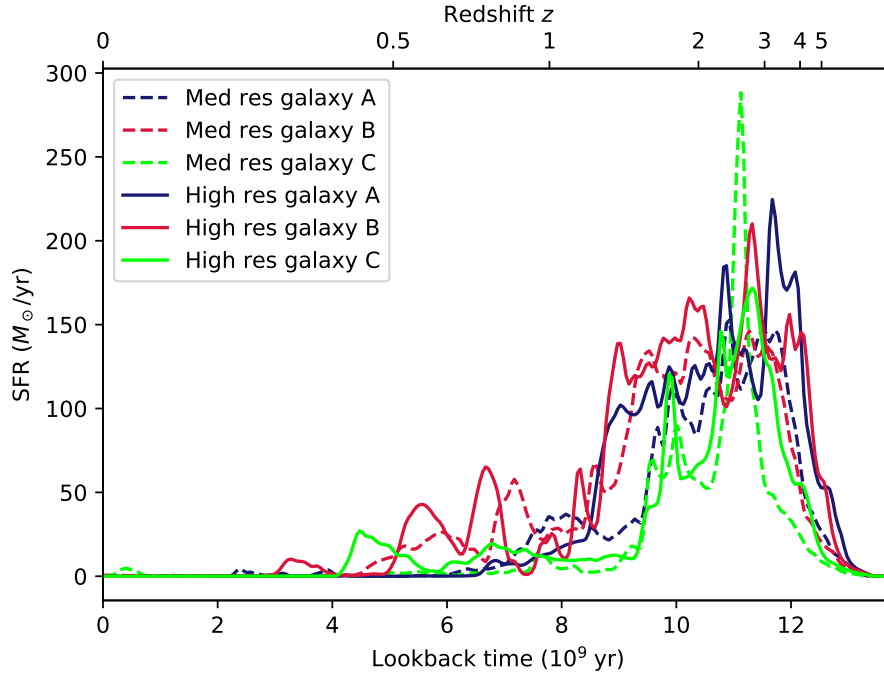


**Figure 5.6:** Stellar formation rates for each zoomed-in galaxy, plotted as a function of lookback time. The lines are created from histograms having a length of 5 Myr, which are then smoothed. The continuous lines represent the high resolution simulations and the dashed lines represent the medium resolution simulations.

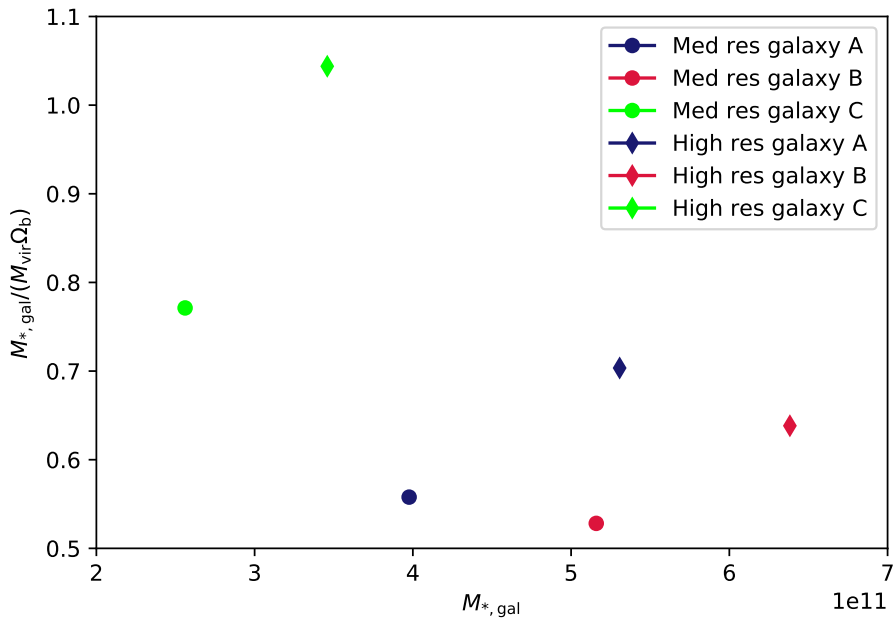


**Figure 5.7:** Galaxy formation efficiencies for each galaxy, plotted with their stellar masses. The cosmological baryon density  $\Omega_b$  is set to 0.045 in the simulations. The diamond and circular markers show the results of the high resolution and the medium resolution zoom-in simulations, respectively.

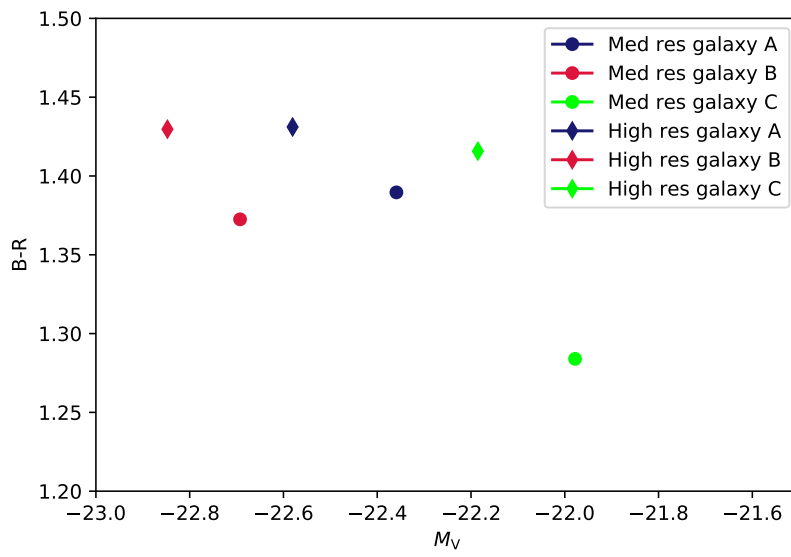


**Figure 5.8:** B-R colors for each simulated galaxy, plotted with each galaxy's absolute magnitude in the V-band. The diamond and circular markers show the results of the high resolution and the medium resolution zoom-in simulations, respectively.

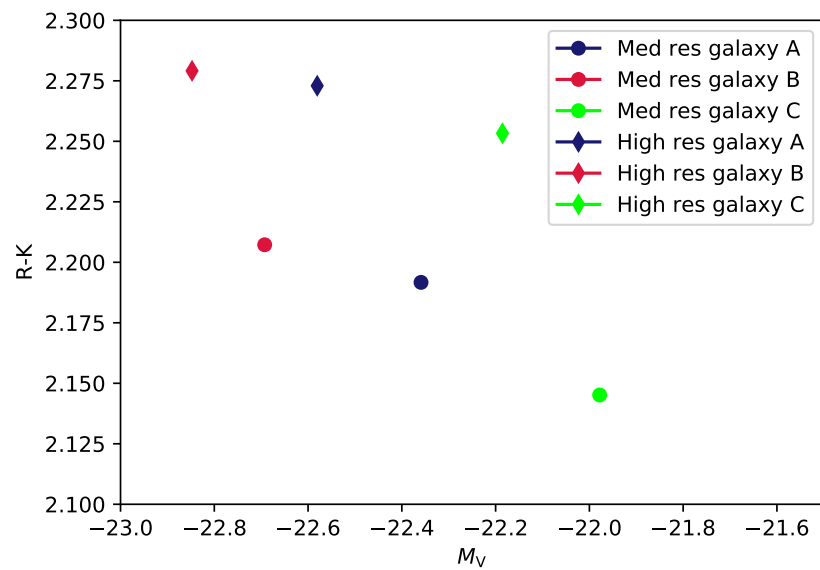


**Figure 5.9:** R-K colors for each simulated galaxy, plotted with each galaxy's absolute magnitude in the V-band. The diamond and circular markers show the results of the high resolution and the medium resolution zoom-in simulations, respectively.

## 6. Simulations with KETJU

## 7. Conclusions

- recap on what was written/studied
- more own thoughts on results
- future missions
- how could the simulations be more realistic (higher resolution, more feedback stuff?)

# Bibliography

- Bertschinger, E. (2001). Multiscale Gaussian Random Fields and Their Application to Cosmological Simulations. *Astrophysical Journal Supplement Series*, 137(1):1–20.
- Brandt, A. (1977). Multi-level adaptive solutions to boundary-value problems. *Mathematics of Computation*, 31(138):333–390.
- Davis, M., Efstathiou, G., Frenk, C. S., & White, S. D. M. (1985). The evolution of large-scale structure in a universe dominated by cold dark matter. *Astrophysical Journal*, 292:371–394.
- Hahn, O. & Abel, T. (2011). Multi-scale initial conditions for cosmological simulations. *Monthly Notices of the Royal Astronomical Society*, 415(3):2101–2121.
- Hoffman, Y. & Ribak, E. (1991). Constrained Realizations of Gaussian Fields: A Simple Algorithm. *Astrophysical Journal Letters*, 380:L5.
- Huchra, J. P. & Geller, M. J. (1982). Groups of Galaxies. I. Nearby groups. *Astrophysical Journal*, 257:423–437.
- Johansson, P. H., Naab, T., & Ostriker, J. P. (2012). Forming Early-type Galaxies in  $\Lambda$ CDM Simulations. I. Assembly Histories. *Astrophysical Journal*, 754(2):115.
- Kwon, Y., Nunley, D., Gardner, J. P., Balazinska, M., Howe, B., & Loebman, S. (2010). Scalable clustering algorithm for n-body simulations in a shared-nothing cluster. In Gertz, M. & Ludäscher, B., editors, *Scientific and Statistical Database Management*, page 132–150. Springer Berlin Heidelberg.
- Marinacci, F., Pakmor, R., & Springel, V. (2014). The formation of disc galaxies in high-resolution moving-mesh cosmological simulations. *Monthly Notices of the Royal Astronomical Society*, 437(2):1750–1775.

- Meza, A., Navarro, J. F., Steinmetz, M., & Eke, V. R. (2003). Simulations of Galaxy Formation in a  $\Lambda$ CDM Universe. III. The Dissipative Formation of an Elliptical Galaxy. *Astrophysical Journal*, 590(2):619–635.
- Mo, H., van den Bosch, F. C., & White, S. (2010). *Galaxy Formation and Evolution*.
- Naab, T., Johansson, P. H., Ostriker, J. P., & Efstathiou, G. (2007). Formation of Early-Type Galaxies from Cosmological Initial Conditions. *Astrophysical Journal*, 658(2):710–720.
- Napolitano, N. R., Romanowsky, A. J., Coccato, L., Capaccioli, M., Douglas, N. G., Noordermeer, E., Gerhard, O., Arnaboldi, M., de Lorenzi, F., Kuijken, K., Merrifield, M. R., O’Sullivan, E., Cortesi, A., Das, P., & Freeman, K. C. (2009). The Planetary Nebula Spectrograph elliptical galaxy survey: the dark matter in NGC 4494. *Monthly Notices of the Royal Astronomical Society*, 393(2):329–353.
- Navarro, J. F. & White, S. D. M. (1994). Simulations of dissipative galaxy formation in hierarchically clustering universes-2. Dynamics of the baryonic component in galactic haloes. *Monthly Notices of the Royal Astronomical Society*, 267(2):401–412.
- Nolthenius, R. & White, S. D. M. (1987). Groups of galaxies in the CfA survey and in cold dark matter universes. *Monthly Notices of the Royal Astronomical Society*, 225:505–530.
- Nurmi, P., Heinämäki, P., Sepp, T., Tago, E., Saar, E., Gramann, M., Einasto, M., Tempel, E., & Einasto, J. (2013). Groups in the Millennium Simulation and in SDSS DR7. *Monthly Notices of the Royal Astronomical Society*, 436(1):380–394.
- Oñorbe, J., Garrison-Kimmel, S., Maller, A. H., Bullock, J. S., Rocha, M., & Hahn, O. (2014). How to zoom: bias, contamination and Lagrange volumes in multimass cosmological simulations. *Monthly Notices of the Royal Astronomical Society*, 437(2):1894–1908.
- Pen, U.-L. (1997). Generating Cosmological Gaussian Random Fields. *Astrophysical Journal Letters*, 490(2):L127–L130.
- Planck Collaboration, Aghanim, N., Akrami, Y., Ashdown, M., Aumont, J., Bacigalupi, C., Ballardini, M., Banday, A. J., Barreiro, R. B., Bartolo, N., Basak, S., Battye, R., Benabed, K., Bernard, J. P., Bersanelli, M., Bielewicz, P., Bock,

J. J., Bond, J. R., Borrill, J., Bouchet, F. R., Boulanger, F., Bucher, M., Burigana, C., Butler, R. C., Calabrese, E., Cardoso, J. F., Carron, J., Challinor, A., Chiang, H. C., Chluba, J., Colombo, L. P. L., Combet, C., Contreras, D., Crill, B. P., Cuttaia, F., de Bernardis, P., de Zotti, G., Delabrouille, J., Delouis, J. M., Di Valentino, E., Diego, J. M., Doré, O., Douspis, M., Ducout, A., Dupac, X., Dusini, S., Efstathiou, G., Elsner, F., Enßlin, T. A., Eriksen, H. K., Fantaye, Y., Farhang, M., Fergusson, J., Fernandez-Cobos, R., Finelli, F., Forastieri, F., Frailis, M., Fraisse, A. A., Franceschi, E., Frolov, A., Galeotta, S., Galli, S., Ganga, K., Génova-Santos, R. T., Gerbino, M., Ghosh, T., González-Nuevo, J., Górski, K. M., Gratton, S., Gruppuso, A., Gudmundsson, J. E., Hamann, J., Handley, W., Hansen, F. K., Herranz, D., Hildebrandt, S. R., Hivon, E., Huang, Z., Jaffe, A. H., Jones, W. C., Karakci, A., Keihänen, E., Keskitalo, R., Kiiveri, K., Kim, J., Kisner, T. S., Knox, L., Krachmalnicoff, N., Kunz, M., Kurki-Suonio, H., Lagache, G., Lamarre, J. M., Lasenby, A., Lattanzi, M., Lawrence, C. R., Le Jeune, M., Lemos, P., Lesgourgues, J., Levrier, F., Lewis, A., Liguori, M., Lilje, P. B., Lilley, M., Lindholm, V., López-Caniego, M., Lubin, P. M., Ma, Y. Z., Macías-Pérez, J. F., Maggio, G., Maino, D., Mandolesi, N., Mangilli, A., Marcos-Caballero, A., Maris, M., Martin, P. G., Martinelli, M., Martínez-González, E., Matarrese, S., Mauri, N., McEwen, J. D., Meinhold, P. R., Melchiorri, A., Menella, A., Migliaccio, M., Millea, M., Mitra, S., Miville-Deschénes, M. A., Molinari, D., Montier, L., Morgante, G., Moss, A., Natoli, P., Nørgaard-Nielsen, H. U., Pagano, L., Paoletti, D., Partridge, B., Patanchon, G., Peiris, H. V., Perrotta, F., Pettorino, V., Piacentini, F., Polastri, L., Polenta, G., Puget, J. L., Rachen, J. P., Reinecke, M., Remazeilles, M., Renzi, A., Rocha, G., Rosset, C., Roudier, G., Rubiño-Martín, J. A., Ruiz-Granados, B., Salvati, L., Sandri, M., Savelainen, M., Scott, D., Shellard, E. P. S., Sirignano, C., Sirri, G., Spencer, L. D., Sunyaev, R., Suur-Uski, A. S., Tauber, J. A., Tavagnacco, D., Tenti, M., Toffolatti, L., Tomasi, M., Trombetti, T., Valenziano, L., Valiviita, J., Van Tent, B., Vibert, L., Vielva, P., Villa, F., Vittorio, N., Wandelt, B. D., Wehus, I. K., White, M., White, S. D. M., Zacchei, A., & Zonca, A. (2020). Planck 2018 results. VI. Cosmological parameters. *Astronomy & Astrophysics*, 641:A6.

Power, C., Navarro, J. F., Jenkins, A., Frenk, C. S., White, S. D. M., Springel, V., Stadel, J., & Quinn, T. (2003). The inner structure of  $\Lambda$ CDM haloes - I. A numerical convergence study. *Monthly Notices of the Royal Astronomical Society*, 338(1):14–34.

- Reed, D. S., Smith, R. E., Potter, D., Schneider, A., Stadel, J., & Moore, B. (2013). Towards an accurate mass function for precision cosmology. *Monthly Notices of the Royal Astronomical Society*, 431(2):1866–1882.
- Röttgers, B., Naab, T., Cernetic, M., Davé, R., Kauffmann, G., Borthakur, S., & Földl, H. (2020). Lyman  $\alpha$  absorption beyond the disc of simulated spiral galaxies. *Monthly Notices of the Royal Astronomical Society*, 496(1):152–168.
- Salmon, J. (1996). Generation of Correlated and Constrained Gaussian Stochastic Processes for N-Body Simulations. *Astrophysical Journal*, 460:59.
- Sirko, E. (2005). Initial Conditions to Cosmological N-Body Simulations, or, How to Run an Ensemble of Simulations. *Astrophysical Journal*, 634(2):728–743.
- Tissera, P. B. & Dominguez-Tenreiro, R. (1998). Dark matter halo structure in CDM hydrodynamical simulations. *Monthly Notices of the Royal Astronomical Society*, 297(1):177–194.
- Weijmans, A.-M., Krajnović, D., van de Ven, G., Oosterloo, T. A., Morganti, R., & de Zeeuw, P. T. (2008). The shape of the dark matter halo in the early-type galaxy NGC 2974. *Monthly Notices of the Royal Astronomical Society*, 383(4):1343–1358.
- Zel'Dovich, Y. B. (1970). Gravitational instability: an approximate theory for large density perturbations. *Astronomy & Astrophysics*, 500:13–18.